Journal of Manufacturing Processes 49 (2020) 214–226

Contents lists available at ScienceDirect

Journal of Manufacturing Processes

journal homepage: www.elsevier.com/locate/manpro

Influence of tool rotational speed on local microstructure, mechanical and corrosion behavior of dissimilar AA2024/7075 joints fabricated by friction stir welding

Chenghang Zhang[a,b], Yu Cao[a,b,*], Guangjie Huang[a,b,*], Qinghui Zeng[c], Yulong Zhu[a,b], Xinde Huang[a,b], Na Li[a,b], Qing Liu[d]

[a] International Joint Laboratory for Light Alloys (MOE), College of Materials Science and Engineering, Chongqing University, Chongqing 400044, PR China
[b] Shenyang National Laboratory for Materials Science, Chongqing University, Chongqing 400044, PR China
[c] College of Mechanical and Electrical Engineering, Chongqing University of Arts and Sciences, Chongqing 402160, PR China
[d] College of Materials Science and Engineering, Nanjing Tech University, Nanjing 211816, PR China

ARTICLE INFO

Keywords:
Aluminum alloys
Friction stir welding
Microstructure
Mechanical properties
Corrosion behavior

ABSTRACT

In this investigation, the local microstructure evolution, mechanical properties and corrosion behavior of the dissimilar friction stir welded AA2024/7075 joints were evaluated as a function of rotational speed. The results showed that the rotational speed mainly affects the local microstructure and performance of the dissimilar joints. Fine equiaxed grains are formed in the nugget zone (NZ). The average grain size decreases in the sequence of shoulder zone (SZ), center zone (CZ) and bottom zone (BZ), and increases with increasing rotational speed. Different types of shear textures are formed at different positions of the NZ, which vary with the rotational speed. The maximum tensile strength of 411.4 MPa is acquired in the joint at 950 rpm, with the welding efficiency of about 87.6 % relative to the AA2024 base material. The fracture position of all the joints is in the lowest hardness zone during tensile tests. Higher corrosion current density presents in the welded zone, which results from the formation of galvanic corrosion. The corrosion behavior of the welded zone is influenced by rotational speed and higher corrosion resistance can be acquired in the joint fabricated at 950 rpm due to the appropriate precipitates density and size.

1. Introduction

Aluminum alloys are an ideal material for light weight in aerospace, transportation and other manufacturing fields because of their low density, high specific strength and excellent corrosion resistance [1]. As a structural material, selecting different materials in disparate parts depends on the performance requirements of actual working conditions, manufacturing process and cost in actual production and application. Accordingly, the welding between dissimilar aluminum alloys is inevitably conducted, especially for the 2xxx and 7xxx aluminum alloys [2]. For instance, AA2024 alloy is mainly used for fabricating various high-load parts and components such as skeleton parts, skins and spars on airplanes [3]. AA7075 alloy is widely employed for the upper skin of the wing, fuselage frame and ribs [4]. As a result of the differences in physical, chemical, metallurgical and thermodynamic properties of AA2024 and AA7075 aluminum alloys, it is particularly difficult to weld these two alloys through fusion welding [5], which can be attributed to the generated welding defects (e.g. solidification cracking and voiding) leading to some poor mechanical performances [6].

As a novel welding technology, friction stir welding (FSW) can realize the seamless welding between 2xxx and 7xxx aluminum alloys [7–9]. In the process of FSW, the welded materials experience drastic plastic deformation and material flow under the friction and extrusion of the tool, finally acquiring a reliable joint [10]. Since FSW has the advantages of no spatter, no need for welding wire and protective gas, and no melting of materials, it can effectively avoid the welding defects such as brittle phase, solidification crack and hole [11]. Consequently, FSW has been widely used in aerospace, high-speed trains and other manufacturing fields [12]. Generally, four zones are formed in the FSW joint, i.e., nugget zone - NZ, thermos-mechanical affected zone - TMAZ, heat affected zone - HAZ and base material - BM. The HAZ is usually located at the regions where the fracture takes place [13,14]. Khan

* Corresponding authors at: International Joint Laboratory for Light Alloys (MOE), College of Materials Science and Engineering, Chongqing University, Chongqing 400044, PR China.
E-mail addresses: yucao928@cqu.edu.cn (Y. Cao), gjhuang@cqu.edu.cn (G. Huang).

https://doi.org/10.1016/j.jmapro.2019.11.031
Received 27 August 2019; Received in revised form 14 November 2019; Accepted 26 November 2019

et al. [15] studied the mechanical properties of similar and dissimilar FSW AA2219-O/7475-T761 joints. The results indicated that dissimilar joints display lowest strength compared to the similar joints and the tensile specimens fracture in the TMAZ and/or HAZ regions of the joints. Prime et al. [16] conducted the residual stress tests of dissimilar AA2024-T351/7050-T7451 joints with the thickness of 25.4 mm and concluded that the peak stress value is about 32 MPa, which is located in the HAZ. Cavaliere et al. [17] performed the FSW of 2.5 mm thick dissimilar AA2024-T3/7075-T6 joints and reported that the line of material flow weakens the fatigue performance of the joints.

The precious researchers mainly focus on the effect of the FSW processing parameters on the microstructure and mechanical properties of the dissimilar joints between 2xxx and 7xxx aluminum alloys. Da Silva et al. [18] found that material flow and mechanical properties of 3 mm thick dissimilar AA2024-T3/7075-T6 joints mainly depend on the welding parameters. They found that high rotational speed produces the typical onion ring-like mixing pattern in the NZ, while low rotational speed results in limited material mixing. Khodir and Shibayanagi [19,20] obtained the maximum tensile strength of dissimilar AA2024-T3/7075-T6 joints with the thickness of 3 mm at the rotational speed of 1200 rpm and the welding speed of 100 mm/min with the AA7075-T6 on the retreating side (RS). Venkateswarlu et al. [21] acquired the optimal welding parameters for dissimilar FSW AA2219/7039 joints. Besides, tool profile and machine variables have an obvious effect on the mechanical properties of the FSW joints [22–24]. Saravanan et al. [25,26] evaluated the influence of D/d ratio (D - shoulder diameter, d - pin diameter) on the microstructure and mechanical properties of dissimilar AA2024-T6/7075-T6 joints with a thickness of 5 mm. They found that the excellent mechanical properties can be acquired using D/d ratio of 3. The clamping system of the FSW equipment also affects the mechanical performance of the dissimilar joints. Hasan et al. [27] found that it is favorable to use the revised backing and clamping system with thermal conductivity under low welding speed. On the basis of these literature findings, the researches aim to the influence of the FSW processing parameters on mechanical properties of the 2xxx and 7xxx dissimilar aluminum alloy FSW joints. Although we also analyzed the microstructure and mechanical properties of the dissimilar AA7075/2024 joints in our previous work [8], there have been few works concerning the local microstructure evolution and corrosion properties of the joints between 2xxx and 7xxx aluminum alloys. Moreover, the microstructural analysis is not thorough because of the uneven thermal deformation state and complex material flow behavior in the NZ of dissimilar joints. Accordingly, it is crucial to fully analyze the local microstructure evolution of different welded zones in the dissimilar FSW joints.

In this work, AA2024-T351 and AA7075-T651 sheets were employed for the friction stir butt welding tests. Electron backscattering diffraction (EBSD) technique was used to investigate the evolution of grain structure and crystal orientation at different areas of the NZ in the dissimilar joints with various rotational speeds. Finally, the mechanical properties and corrosion behavior of the dissimilar joints were also studied to provide a theoretical basis for promoting the performances of FSW joints.

2. Experimental procedure

The welding BMs were AA2024-T351 and AA7075-T651 aluminum alloy sheets with dimensions of 300 mm × 40 mm × 5 mm. Table 1 exhibits the nominal chemical compositions of the two BMs. The two BMs were butt-welded by the FSW machine (FSW-LM-AM16-2D) at constant welding speed of 100 mm/min and plunge depth of 0.03 mm, for various rotational speeds ranging from 600 rpm, 950 rpm and 1650 rpm. The FSW tool was characterized by a concave shoulder of 15 mm in diameter, as well as a threaded probe with 3.8 mm in tip diameter and 5 mm in length. The welding direction (WD) was perpendicular to the rolling direction (RD) of the two BMs. The AA2024 BM was located on the advancing side (AS), and AA7075 BM was placed on the RS. The tilting angles of the tool were 2.5° during FSW.

Table 1
Chemical composition of AA2024-T351 and AA7075-T651 (in wt.%).

	Si	Fe	Cu	Mn	Mg	Cr	Zn	Ti	Al
2024-T351	0.05	0.17	4.5	0.6	1.4	0.01	0.03	0.02	Bal.
7075-T651	0.05	0.19	1.7	0.04	2.4	0.2	5.8	0.03	Bal.

The samples were cut along the cross section of the joints after welding. According to the standard metallographic methods, the specimens were ground with 400, 800, 1200, 2000, 3000 and 4000 grit silicon carbide sandpapers in turn, then followed by mechanical polishing using diamond polishing paste of 2 μm and 0.5 μm. The macroscopic morphology of the joint was observed after chemical corrosion with Keller's reagent. The microstructure observations were conducted by applying field emission scanning electron microscopy (FESEM, JEOL JSM-7800F). The electron backscatter diffraction (EBSD) technique was performed on the SEM (TESCAN MIRA3) equipped with a HKL-EBSD system. The microstructure of the welded zone were analyzed using a step size of 0.3 μm. Before EBSD, the polished samples were electropolished in an electrolyte (perchloric acid : ethanol = 1:9, vol.%) at 2 − 5 °C and 15 V for 100 s. The Channel 5 software was employed to analyze the EBSD data. The precipitated phases were detected by using transmission electron microscope (TEM, FEI TECNAI G2 F20), which was operated at 200 kV. The TEM samples were ground to 60 μm and rushed into 3 mm in diameter, and then electropolished in a 25 % HNO_3 methanol solution at − 30 °C using the twin-jet technique.

For mechanical measurements, the tensile samples with a gauge width of 4 mm and length of 40 mm (Fig. 1a) were cut along the cross-section of the dissimilar joints. Afterwards, the samples were ground parallel to the orientation of the primary load to eliminate the influence of stress concentration and the heterogeneous distribution of thickness arisen from the FSW. Tensile tests were conducted by a Shimadzu AG-X plus universal testing machine at a crosshead speed of 1 mm/min. Three tensile samples were cut from each joint to ensure the reliability of tensile data. Vickers micro-hardness tests were implemented along the center line of thickness in the dissimilar joints using digital microhardness tester (MH-3) with a load of 200 g for 10 s.

For corrosion tests, immersion tests were performed in 3.5 wt.% NaCl solution for 24 h. The potentiodynamic polarization test was performed by using Gamry electrochemical system (Gamry, United States) at room temperature. Prior to the test, the specimens were cut into trapezoids according to the basin shape of the NZ, as displayed in Fig. 1b. The side and back of the specimens after cut were sealed by insulating epoxy resin in order that the surface was only exposed to the solution. A three-electrode system, which consists of the samples as the

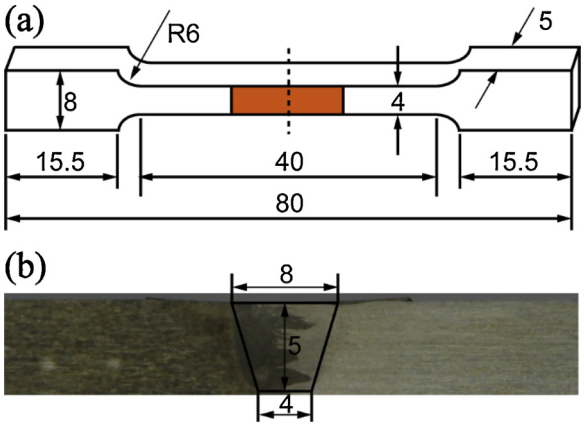

Fig. 1. Test sizes: (a) tensile specimens and (b) corrosion specimens.

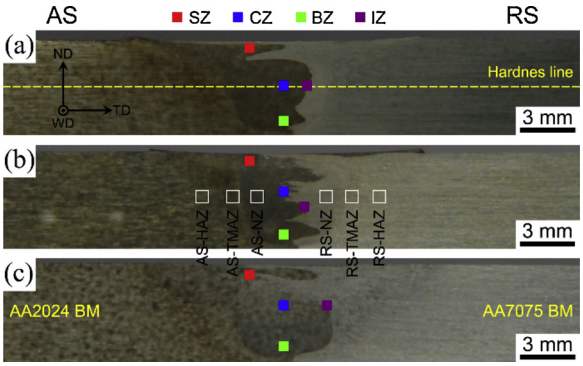

Fig. 2. The macro-morphologies of the dissimilar AA2024/7075 joints: (a) 600 rpm, (b) 950 rpm and (c) 1650 rpm.

working electrode, a platinum sheet as counter electrode and a saturated calomel electrode (SCE) as reference electrode, was employed. The scanning range was −1.6–0.2 V (vs SCE) at a scan speed of 1 mV/s. Corrosion potential (E_{corr}) and corrosion current density (I_{corr}) can be evaluated by conducting the Tafel-type fit of the data from the polarization curves. Three test samples were measured in each sample to reduce the error.

3. Results and discussion

3.1. Cross-sectional morphologies of the dissimilar joints

Fig. 2 exhibits the macroscopic morphologies of cross-section in the dissimilar joints at different rotation speeds. Welding defects such as holes or tunnels are hardly observed in the dissimilar joints. Due to the different reactions of the two BMs with the Keller' reagent, the dark and light areas represent AA2024 and AA7075 BMs, respectively. Therefore, it can be clearly seen that the two BMs undergo a significant plastic mixing flow in the NZ under the agitation of the tool and exhibit a tendency of materials flowing from AS (AA2024 BM) to RS (AA7075 BM). Rodriguez et al. [28] also found this phenomenon in the dissimilar FSW AA6061/7050 joints. Furthermore, the NZ is composed of a mixture of materials on the AS and RS, and the AS materials occupy a major portion. According to the material flow characteristics in the NZ, EBSD test was carried out at different positions of the NZ, which can be mainly divided into four zones: shoulder zone (SZ), center zone (CZ), bottom zone (BZ) and interface zone (IZ). The specific region locations of EBSD tests are marked with different colored in Fig. 2.

3.2. Microstructure of the dissimilar joints

3.2.1. Base materials

The initial grain structure, misorientation angle distributions and (111) pole figure (PF) of the two BMs are shown in Fig. 3. Low angle grain boundaries (LAGBs, 2-15°) and high angle grain boundaries (HAGBs, over 15°) are represented as black and white lines, respectively. The two BMs mainly contain substantial elongated grains caused by rolling process, and the width of AA2024 is larger than that of AA7075 in the vertical direction (Fig. 3a and d). As shown in Fig. 3b and e, a larger number of HAGBs are distributed in AA2024 BM with the volume fraction of 73.8 %, while AA7075 BM mainly contains LAGBs with the volume fraction of 48.2 %. Plastic deformation is prone to generate the rotation of grains, resulting in the formation of some texture. On the basic of the (111) PFs in Fig. 3c and f, the $\{001\}\langle100\rangle$ Cube texture component is dominant for AA2024 BM, while $\{011\}\langle211\rangle$ Brass and $\{123\}\langle634\rangle$ S texture components can be found in AA7075 BM.

Due to the asymmetry of the joints, the welded zones of the dissimilar joints can be divided into six regions, as shown in Fig. 2 (indicated by white square box). AS (RS)-HAZ, AS (RS)-TMAZ, AS (RS)-NZ represent the HAZ, TMAZ and NZ on the AS or RS, respectively. Fig. 4 displays the distribution of precipitations in the two BMs and the six above-mentioned regions. Compared to the two BMs (Fig. 4a and b), larger precipitated particles can be observed in the AS (RS)-HAZ (Fig. 4c and f) and AS (RS)-TMAZ (Fig. 4d and g). This can be ascribed to the heat input produced by FSW, resulting in the coarsening of second phases in the HAZ and TMAZ. Since the HAZ only suffers some thermal cycles without any plastic deformation, the grain structures in the AS/ RS-HAZ resemble their corresponding BMs. The TMAZ is located between the NZ and HAZ. The primary grains in the TMAZ are heavily distorted (marked by the pink arrows in Fig. 4d and g) under plastic deformation, showing a ring-shaped and stretched trend upward the periphery of the NZ (Fig. 4d and g). As can be observed in Fig. 4e and h, both AS-NZ and RS-NZ contain bulk fine second phases since the initial second phases in the corresponding BMs are broken into fine particles and then re-distributed in the NZ by the agitation and rotation of the tool [29].

Fig. 5 displays the bright field TEM images of the two BMs, the AS-HAZ and RS-HAZ in the joint at 600 rpm. Compared to the two BMs in Fig. 5a and c, the precipitate distribution in the AS/RS-HAZ is non-uniform with a mixture of coarse and fine precipitates (Fig. 5b and d). Partial coarsening precipitates are found in the AS-HAZ due to the HAZ experiencing high peak temperature [7]. The fine acicular (marked by the blue arrows in Fig. 5b) and granular precipitate phases (marked by the ellipses in Fig. 5d) within the grains can be observed in the AS-HAZ and RS-HAZ, respectively. This can be ascribed to the fact that the dissolution of partial precipitations leads to the inhomogeneous re-precipitation during cooling [13].

3.2.2. Shoulder zone (SZ)

The EBSD results of the SZ in the joints with three rotational speeds are exhibited in Fig. 6. Apparently, fine lamellar and partial equiaxed grains are formed in the SZ (Fig. 6a, d and g) compared to the initial lath-like grains in the BMs (Fig. 3a and d). During FSW, the initial grains in the BMs are broken into lamellar grains under the combined action of frictional heat and plastic deformation. The direction of black arrows in Fig. 6a, d and g indicates obvious flow trend in the SZ under the shear stress produced by the tool rotation. According to misorientation angle distributions in Fig. 6b, e and h, the volume fraction of HAGBs in the SZ increases slightly with the increase of rotational speed. Besides, the average grain size of the SZ in the joints at the rotational speed of 600, 950 and 1650 rpm was calculated to be 1.87 ± 0.96 μm, 2.75 ± 1.53 μm and 3.38 ± 2.01 μm, respectively.

Texture evolution is closely associated with the deformation mechanism. The process of FSW is similar to torsion or extrusion, and a simple shear is the major deformation mode [30]. Thus, some typical shear textures are formed after shear deformation, which has been documented to be the {hkl} < 110 > fiber and {111} < uvw > fiber in FCC metals [31]. The locations of ideal shear textures along these fibers are demonstrated in Fig. 7 by the (111) PF projected on the SD-SPN plane (SD is the shear direction, and SPN is the shear plane normal) and orientation distribution function (ODF). The specific texture components are respectively denoted as [32]: $\{111\}\langle\bar{1}\bar{1}2\rangle$ A_1^*, $\{111\}\langle11\bar{2}\rangle$ A_2^*, $\{1\bar{1}1\}\langle110\rangle$ A, $\{\bar{1}1\bar{1}\}\langle\bar{1}\bar{1}0\rangle$ $\bar{A}$, $\{1\bar{1}2\}\langle110\rangle$ B, $\{\bar{1}1\bar{2}\}\langle\bar{1}\bar{1}0\rangle$ $\bar{B}$ and $\{001\}\langle110\rangle$ C. Fig. 3c, f and i display the (111) PF and ODF of the SZ in the joints with three different rotational speeds. As can be seen, the SZ in the joint at 600 rpm mainly shows C texture component. $B/\bar{B}$ textures are formed in the SZ of the joint fabricated at 950 rpm. While A_1^*, A_2^* and little C textures can be found in the SZ of the joint produced at 1650 rpm. In addition, the texture intensity in the SZ of the three joints decreases with the increasing rotational speed.

3.2.3. Center zone (CZ)

Fig. 8 displays the EBSD data of the CZ in the joints at three rotational speeds. It can be observed from the orientation distribution maps in Fig. 8a, d and g that many fine equiaxed grains are generated in the

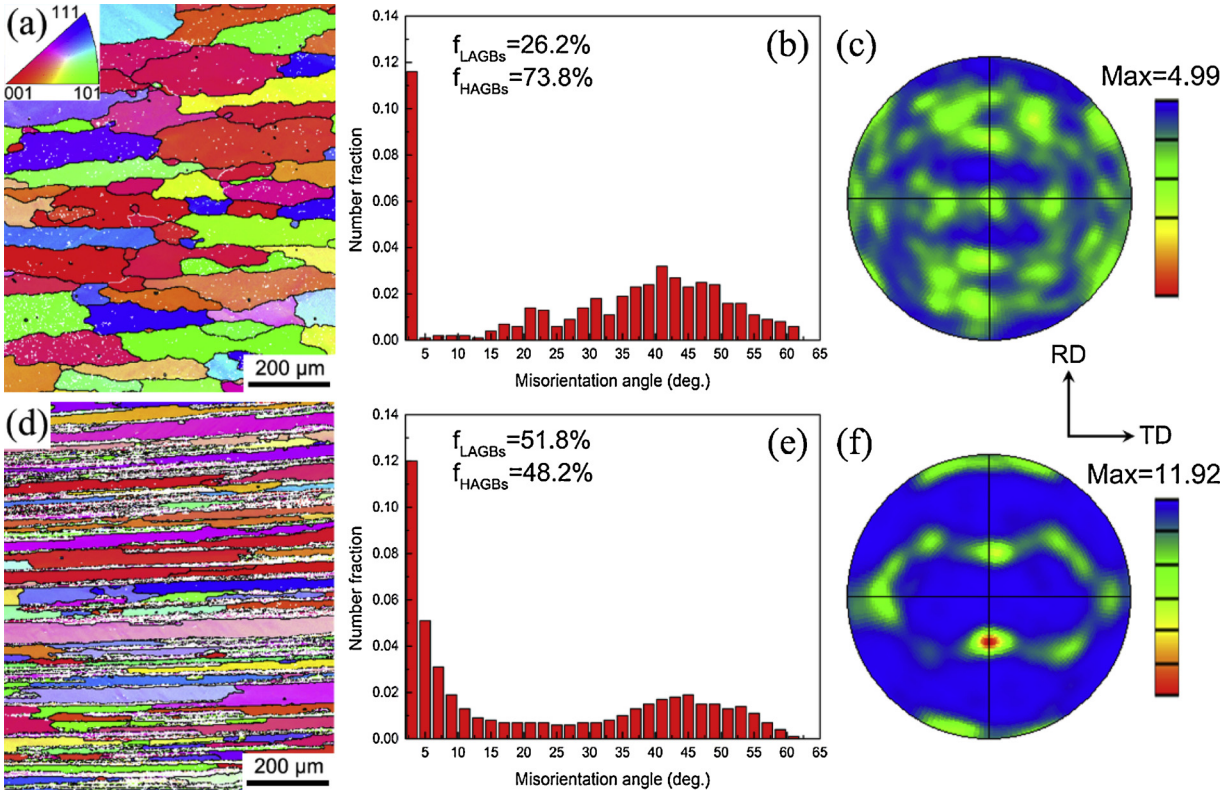

Fig. 3. Orientation distribution maps, misorientation angle distributions and (111) PF of the two BMs: (a–c) AA2024 and (d–f) AA7075.

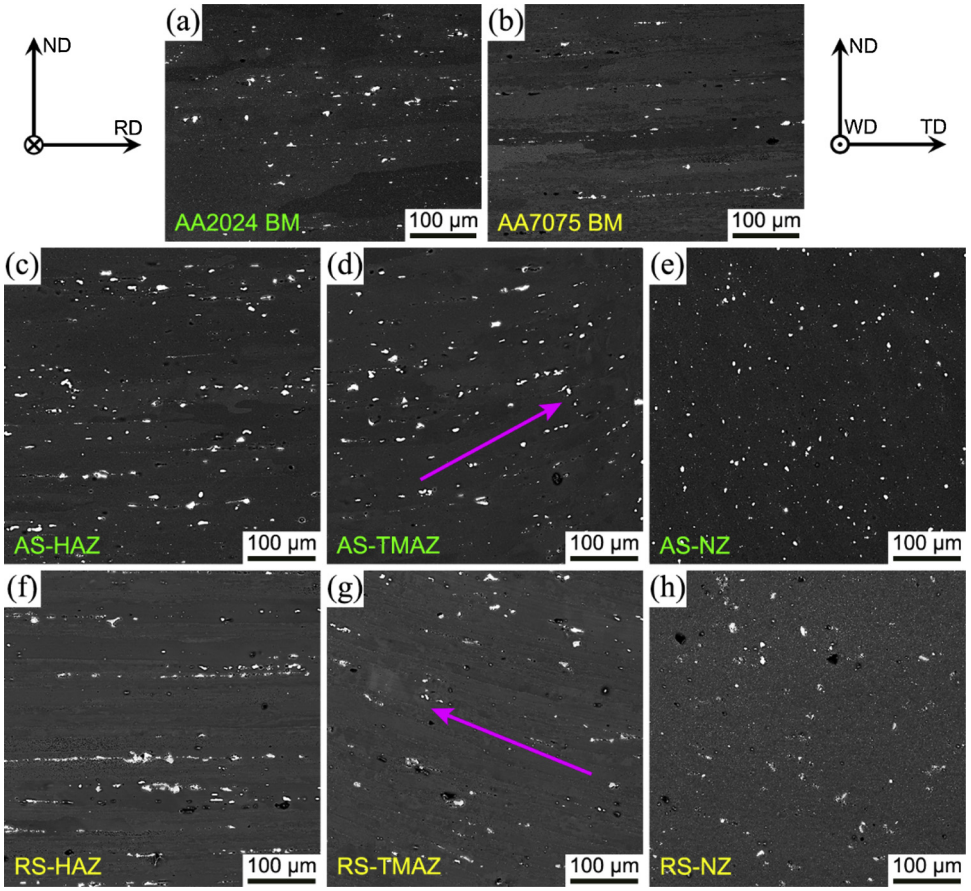

Fig. 4. SEM images of the precipitated phases in (a) AA2024 BM, (b) AA7075BM and welded areas of the joint at 600 rpm (c) AS-HAZ, (d) AS-TMAZ, (e) AS-NZ, (f) RS-HAZ, (g) RS-TMAZ and (h) RS-NZ.

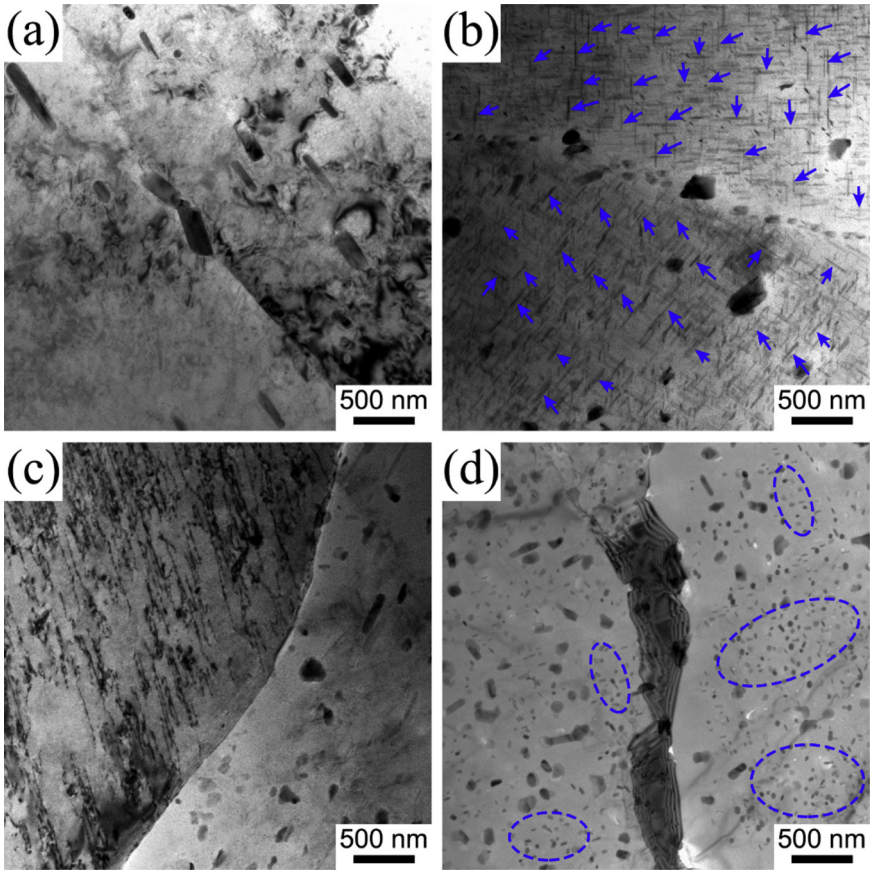

Fig. 5. TEM images showing the precipitation distribution in (a) AA2024 BM, (b) AS-HAZ (c) AA7075 BM and (d) RS-HAZ of the joint at 600 rpm.

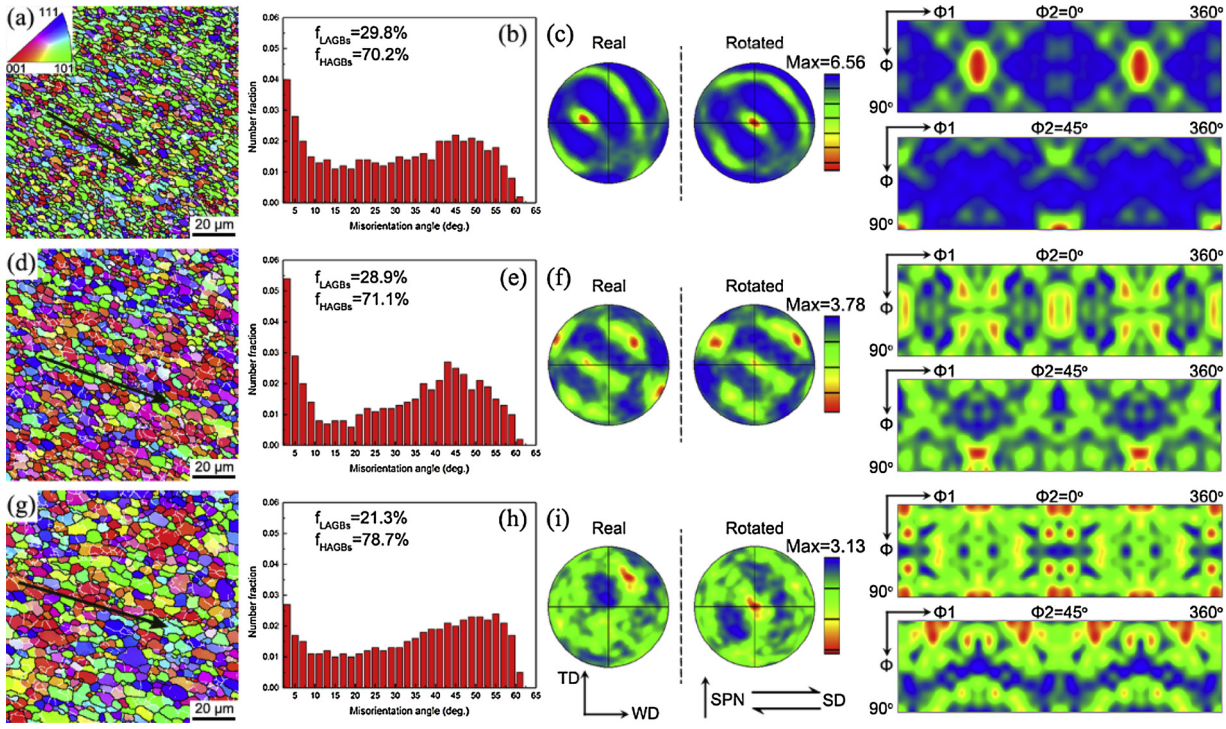

Fig. 6. Orientation distribution maps, misorientation angle distributions and the (111) PF and ODF of the SZ: (a–c) 600 rpm, (d–f) 950 rpm and (g–i) 1650 rpm.

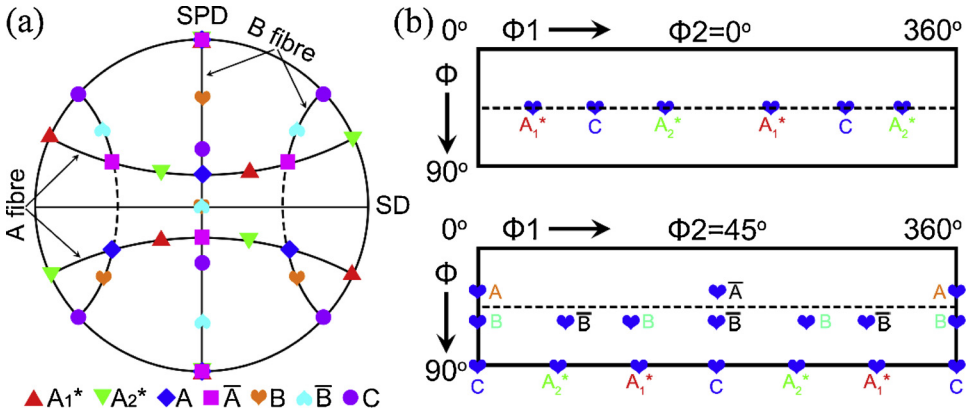

Fig. 7. Ideal orientations of FCC materials at simple shear in (a) (111) PF and (b) ODF (Φ2 = 0° and 45°).

CZ of the joints. It can be implied that complete dynamic recrystallization takes place due to the function of large strain rate and high temperature under the friction and agitation of the FSW tool. By comparing the misorientation angle distributions in Fig. 8b, e and h, as the rotational speed increases from 600 to 1650 rpm, the volume fraction of LAGBs decreases from 17.1%–10.9%. Besides, the average grain size of the CZ is prone to increase with the increasing rotational speed, which are 1.83 ± 0.94 μm, 1.86 ± 0.79 μm and 3.13 ± 1.67 μm in turn. The (111) PF and ODF of the CZ in three joints are indicated in Fig. 8c, f and i, respectively. The CZ in the joints produced at 600 and 1650 rpm mainly contains *C* texture component and a small amount of $A/\bar{A}$ texture components can also be found at 600 rpm, while $B/\bar{B}$, A_1^* and A_2^* texture components are formed in the CZ of the joint at 950 rpm.

3.2.4. Bottom zone (BZ)

The EBSD results of the BZ in the joints at three rotational speeds are exhibited in Fig. 9. By means of statistical analysis in Fig. 9a, d and g, the average grain size of the BZ in all the joints is respectively 1.03 ± 0.48 μm, 1.27 ± 0.56 μm and 1.62 ± 0.83 μm from 600 to 1650 rpm. It is concluded that the rotational speed has little influence on the grain size of the BZ in the joint. Besides, finer grains can be observed in the BZ compared to that of the SZ (Fig. 6a, d and g) and CZ (Fig. 8a, d and g). The NZ is only affected by the agitation action of the tip of the tool pin, contributing to the poor plastic flow behavior. Moreover, the BZ is in contact with the bottom plate, leading to faster heat dissipation compared with other regions. Consequently, insufficient deformation and low peak temperature could result in the fact that the fragmental grains have no time to grow up and thus form the finer grain structure. The misorientation angle distributions in Fig. 9b, e and h indicate that the volume fraction of LAGBs in the BZ increases slightly with the increment of the rotational speed. As can be observed in Fig. 9c, f and i, the texture components of the BZ at three rotational speeds is mainly A_1^* and A_2^*, *C*, $B/\bar{B}$, respectively. The texture intensity is weaker in the BZ of the joint at 1650 rpm compared to other joints.

3.2.5. Interface zone (IZ)

Fig. 10 exhibits the EBSD data of the IZ in the joints at three rotational speeds. The grains distribution before and after removal of large grains (> 2 μm) can be seen in Fig. 10a, d and g. Considering the

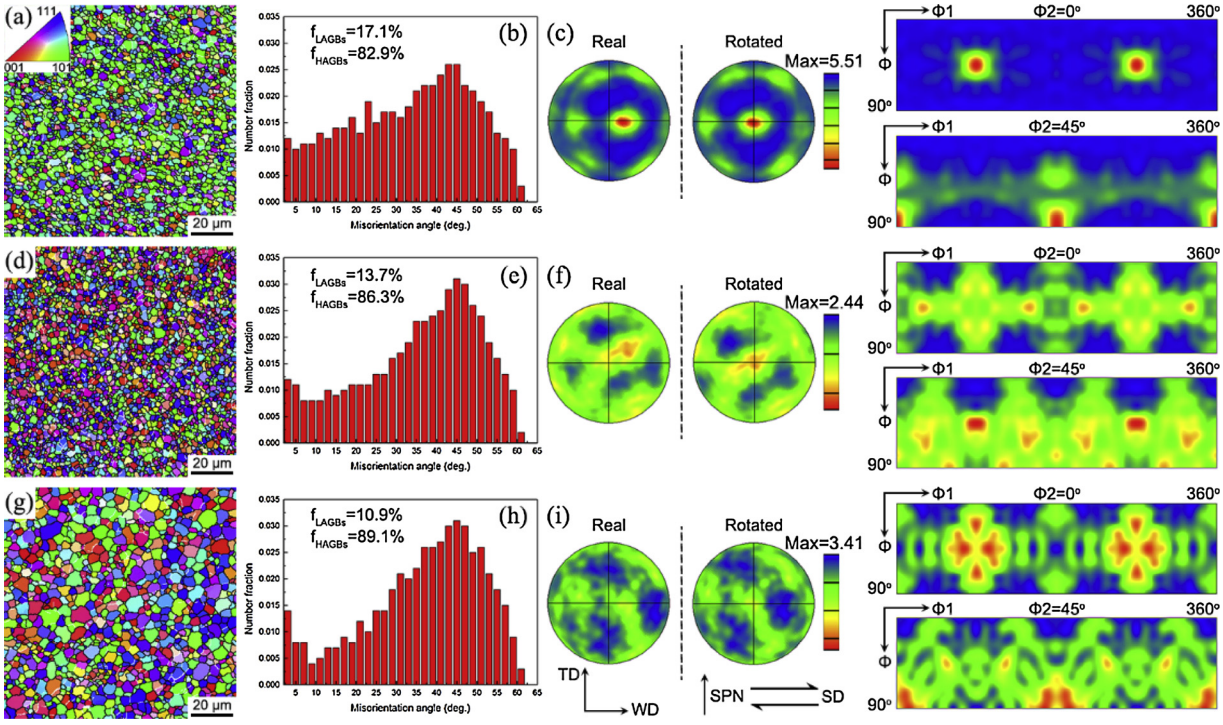

Fig. 8. Orientation distribution maps, misorientation angle distributions and the (111) PF and ODF of the CZ: (a–c) 600 rpm, (d–f) 950 rpm and (g–i) 1650 rpm.

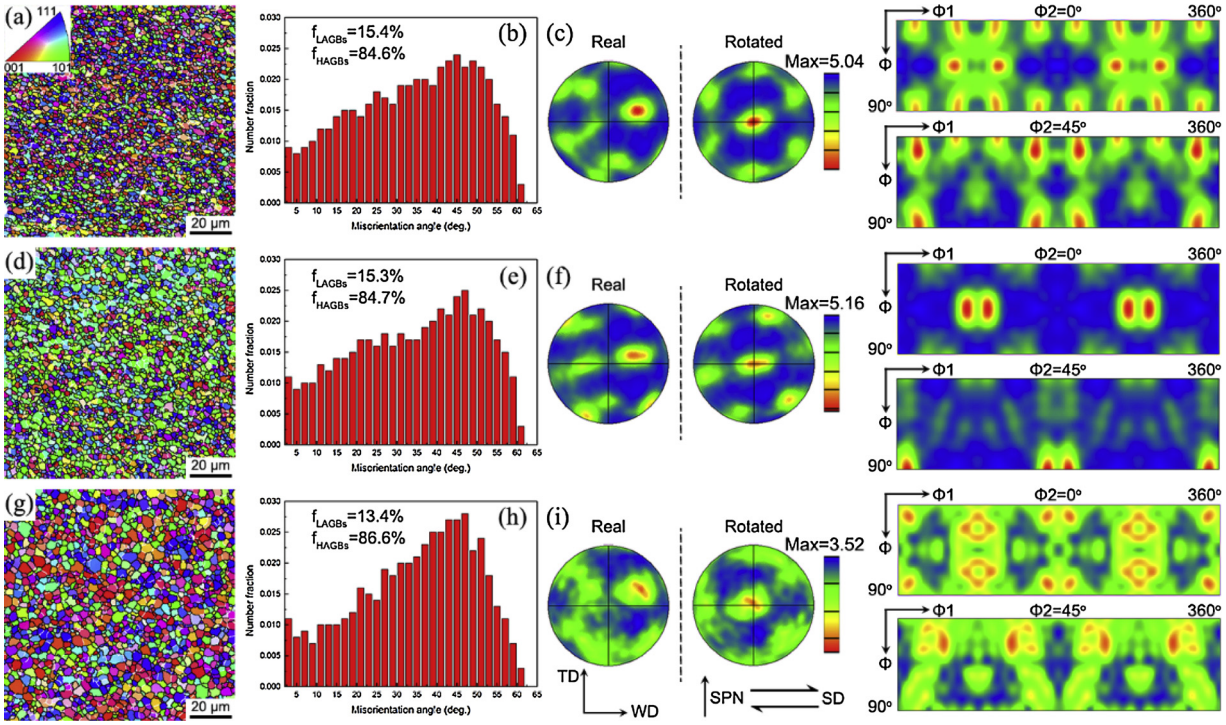

Fig. 9. Orientation distribution maps, misorientation angle distributions and the (111) PF and ODF of the BZ: (a–c) 600 rpm, (d–f) 950 rpm and (g–i) 1650 rpm.

statistical distribution of grain size in Fig. 11, it is found that small grains are interspersed with large grains (Fig. 10a), indicating that insufficient grain crush presents in the IZ of the joint at 600 rpm. However, the grain distribution at 950 rpm is relatively uniform (Fig. 10d), which demonstrates the occurrence of adequate grain fragmentation. With the rotational speed increases up to 1650 rpm, the number of fine grains in the IZ is significantly reduced and some coarse grains are also generated in the IZ (Fig. 10g). Thus, it implies that the rotational speed has an obvious impact on the microstructure of the IZ during FSW. The misorientation angle distributions in Fig. 10b, e and h show that the volume fraction of LAGBs in the IZ of the joint at 950 and 1650 rom is much lower than that of the joint at 600 rpm. This is because higher rotational speed produces higher heat input, resulting in heavy consumption of more dislocation and substructure at high temperature, and then decreasing the volume fraction of LAGBs. Meanwhile, higher temperature causes part of grains to grow up. As depicted in Fig. 10c, f and I, the IZ in the joints at 600 and 950 rpm mainly contains A_1^* and A_2^* texture components, while $B/\bar{B}$ texture components are formed at 1650 rpm.

3.2.6. The difference of grain size

Compared to the two BMs in Fig. 3a and d, significantly refined grains can be found at different regions (SZ, CZ, BZ and IZ) of the NZ. During FSW, recrystallization temperature can be approached due to the large amounts of heat input produced by the friction between the tool and the welded material. Moreover, many dislocations generated by severe plastic deformation are accumulated to a certain extent, which could induce a large number of nucleation sites to facilitate

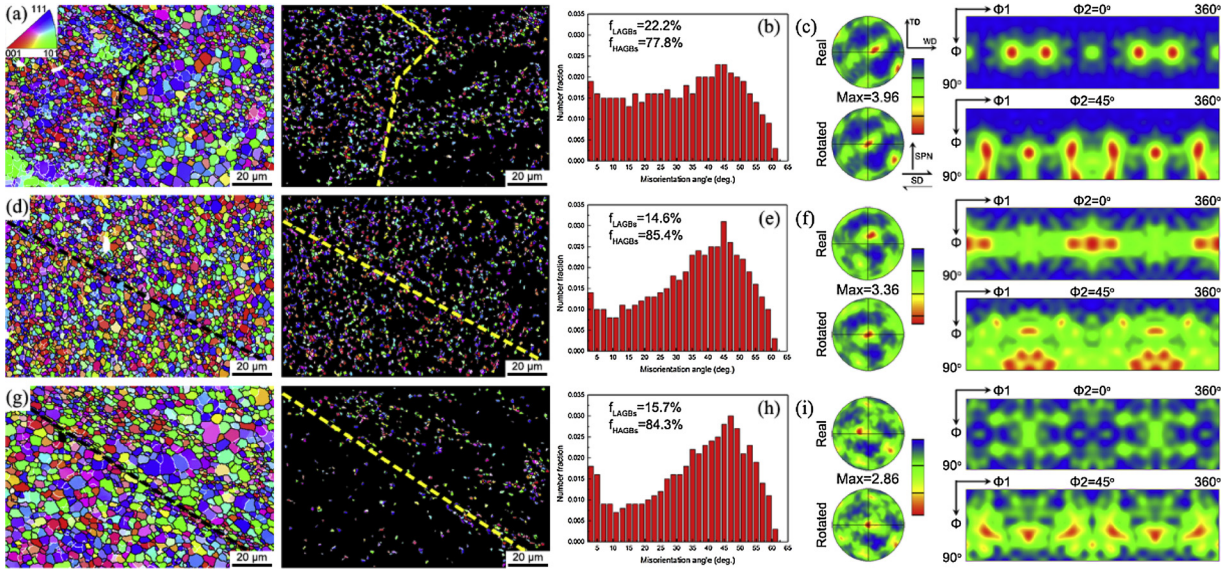

Fig. 10. Orientation distribution maps, misorientation angle distributions and the (111) PF and ODF of the IZ: (a–c) 600 rpm, (d–f) 950 rpm and (g–i) 1650 rpm.

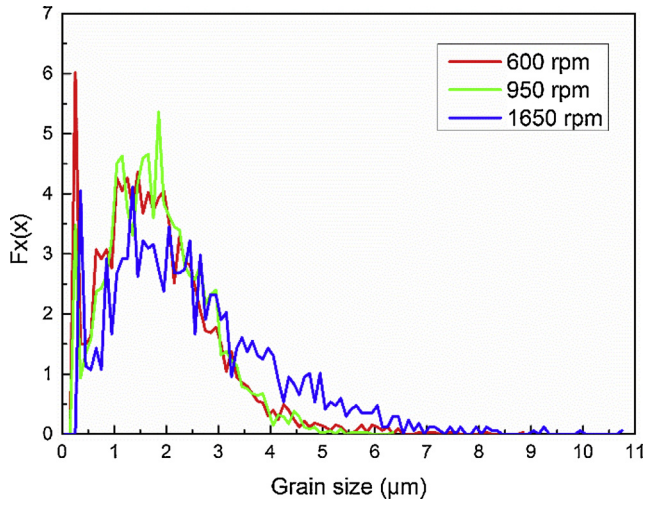

Fig. 11. Grain size distribution maps of the IZ.

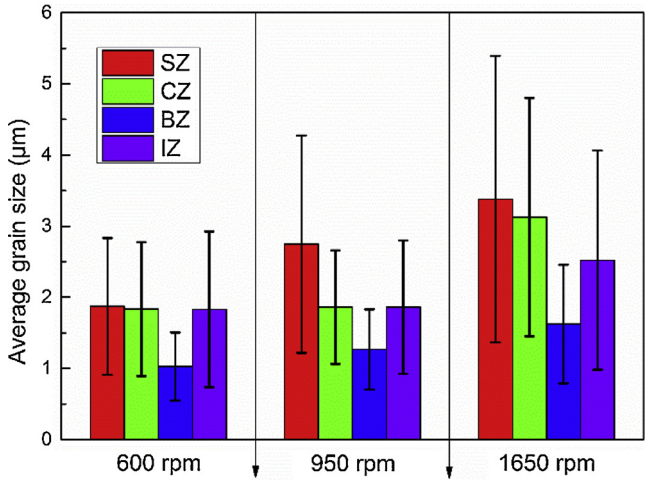

Fig. 12. Statistical charts of the average grain size in various zones of the NZ.

recrystallization [4,13]. In addition, it can be observed that the SZ, CZ, BZ and IZ do not experience full dynamic recrystallization owing to the insufficient strain and/or temperature. The dynamic recovery (DRV) readily occurs due to the fact that the stacking fault energy (SFE) of aluminum is high (approx. 166 mJ · m^{-2}) [33].

Significant differences can also be observed for the grain size of different regions in the NZ. According to the above-mentioned EBSD results (Fig. 6, 8–10a, d, g and Fig. 12), the average grain size of different regions in the NZ of all the joints decreases sequentially from the shoulder region to the bottom region along the direction of plate thickness, namely SZ, CZ and BZ. This is because the temperature of weld surface is higher than that of the bottom region in the NZ. Besides, the diameter of the tool pin gradually decreases from the root to the tip, resulting in different heat input for different parts in the welds. Compared with other regions in the NZ, more heat input is generated in the SZ, where the grains also have sufficient time to grow. However, the BZ is in contact with the bottom plate during welding with a higher rate of heat loss. As a result, less heat is produced in the BZ, which finally generates the microstructure of fine grains.

In view of FSW as a thermomechanical process, the recrystallized grain size can be assessed qualitatively by using the Zener-Hollomon parameter (Z parameter). The dynamically recrystallized grain size (D) is inversely related with the Z parameter as [34]:

$$D = \frac{1}{a + b\ln(Z)} \tag{1}$$

Table 2
Calculated values of peak temperature, strain rate and Zener-Hollomon parameter at various tool rotational speeds.

Rotational speed (rpm)	Peak temperature (K)	Strain rate (1/s)	Z parameter (*10^{15})
600	594.0	20.93	2.508
950	621.9	33.14	3.431
1650	657.2	57.56	4.983

In which both a and b are material constants. The Z parameter can be expressed as [35]:

$$Z = \dot{\varepsilon}\exp(\frac{Q}{RT}) \tag{2}$$

In which $\dot{\varepsilon}$, Q, R and T are the strain rate, the activation energy, the gas constant and deformation temperature, respectively. The Q value of 148.88 kJ/mol was employed according to Carlone et al. [36]. The friction stir processing was simulated by Chang et al. [37], proposing that all the materials in the NZ or dynamically recrystallized zone (DRZ) undergo plastic flow of materials. By adopting a torsion deformation type, the strain rate is calculated as:

$$\dot{\varepsilon} = \frac{R_m 2\pi r_e}{L_e} \tag{3}$$

Where, R_m refers to average rate of material flow, about considered as half of the rotational speed by a line assumption. L_e is about $\pi/4$ of the shoulder radius, which represents the effective depth of the DRZ, r_e is about $\pi/4$ of the plunge depth, which denotes the valid radius of the DRZ. T is the peak temperature (T_p) of the NZ, which can be evaluated by the following formula [38]:

$$\frac{T_p}{T_m} = K(\frac{\omega^2}{V \times 10^4})^{\alpha} \tag{4}$$

Where, T_m is the melting point of material, ω is the rotational speed and V is the welding speed. Both K and α are constants, which can be assessed as 0.7 and 0.05 [39], respectively.

Table 2 summarizes the calculation results of $\dot{\varepsilon}$, T_p and Z parameter. It is clearly observed that the $\dot{\varepsilon}$ increases from 20.93 to 57.56 s^{-1} with the increment of the rotational speed from 600 to 1650 rpm. Regardless of other processing parameters, higher $\dot{\varepsilon}$ leads to the increase of Z parameter, generating finer D. However, Fig. 12 indicates that the average grain size of different regions in the NZ of the joints increases with the increment of rotational speed. Besides, enhancing the rotational speed from 600 to 1650 rpm promotes the temperature from 594.0–657.2 K, which produces high D. Accordingly, the temperature has the predominant impact on the grain size of the different regions in the NZ of the joints.

3.2.7. The difference of misorientation angle distribution

As demonstrated in Figs. 6, 8–10b, e and h, the volume fraction of LAGBs in the SZ, CZ, BZ and IZ in the joints at all the three rotational speeds is reduced compared to the AA7075 BM (Fig. 3e). Due to high temperature thermal cycle and violent plastic deformation caused by the friction and agitation of the tool, dynamic recrystallization occurs in the NZ by consuming some dislocations and substructures [7]. Finally, the volume fraction of LAGBs is obviously decreased.

Besides, the volume fraction of LAGBs in the different regions (SZ, CZ, BZ and IZ) of the NZ decreases with the increment of the rotational speed, which results from the difference in both the introduced plastic strain and heat input evolution with various rotational speeds. The local misorientation maps can be used to further reveal the orientation information as shown in Fig. 13, which corresponds to the regions of the orientation distribution maps (Figs. 6, 8–10a, d and g). The local misorientation maps are focused on the analysis point in the 3 × 3 grid and shows the average misorientation value between the point and the

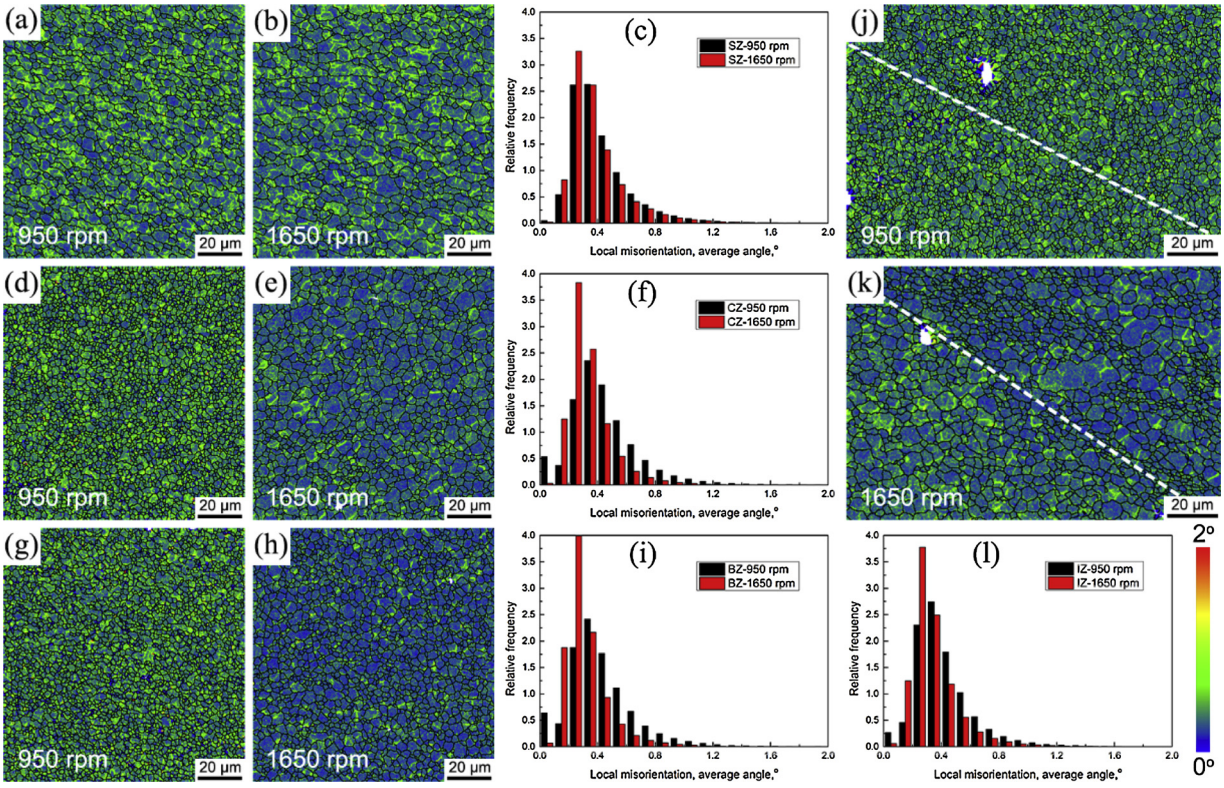

Fig. 13. Local misorientation maps of (a & c) SZ, (d & f) CZ, (g & i) BZ and (j & l) IZ in the NZ of the dissimilar joints.

adjacent eight points [40]. Thereinto, the local misorientation of more than 2° is discarded. These maps illustrate the deformation-induced local orientation gradients within the grains, thus recrystallized grains and local deformation energy can be described [41]. Moreover, the local lattice curvature influences the local misorientation angle, which are tightly linked to the so-called geometrically necessary dislocation density [42,43]. As a consequence, the dislocation density can be calculated by using the local misorientation θ_{loc} [44,45]:

$$\rho = \frac{\alpha\theta_{loc}}{ndb} \tag{5}$$

Where, α is the grain boundary parameters, b is the Burgers vector, n is the defined area size, d is the step size of EBSD measurements. The increasing of the local misorientation corresponds with the increasing in the dislocation density. As demonstrated from the comparison in Fig. 13, the local misorientation of the different regions (SZ, CZ, BZ and IZ) in the welded zone of the joint fabricated at 950 rpm is higher than that of the joint at 1650 rpm. Significant dynamic recrystallization takes place in the NZ of the joint fabricated at 1650 rpm by consuming more dislocations and substructures, leading to lower local misorientation in the NZ.

3.2.8. The difference of texture components

During FSW, the welded materials are subjected to shear deformation under the action of the tool, forming the simple shear texture in the welded zone of the joints. The formation of simple shear texture results from the final severe deformation in the material, caused by the trailing edge of the tool probe during FSW [46]. Based on the results in Figs. 6, 8–10c, f and I and compared to that in the BMs (Fig. 3c and f), the weak texture intensity presents in the welded zone of three joints. The texture components at different regions of the NZ are various for the same joints, and different texture components are also formed at the same position in the NZ of the different joints. These indicate that FSW creates an inhomogeneous texture distribution at different regions in the NZ, meaning that uneven deformation occurs in the NZ during FSW, which are influenced by the shoulder and the probe. This may have an effect on the integrity of the joints in subsequent performance. Shen et al. [47] clarified that the texture components are directly associated with the magnitude of shear strain. In short, A_1^* and A_2^* texture components are produced at lower strains. With the sustained strain, C component can be mostly found at a shear strain of 10–16. Eventually, B and $\bar{B}$ texture components are predominant at a least shear strain of 20 or higher. Therefore, it can be concluded that the upper zones (SZ and CZ) of the welds produces higher strain compared to the bottom zone. Besides, higher rotation speed also results in higher strain.

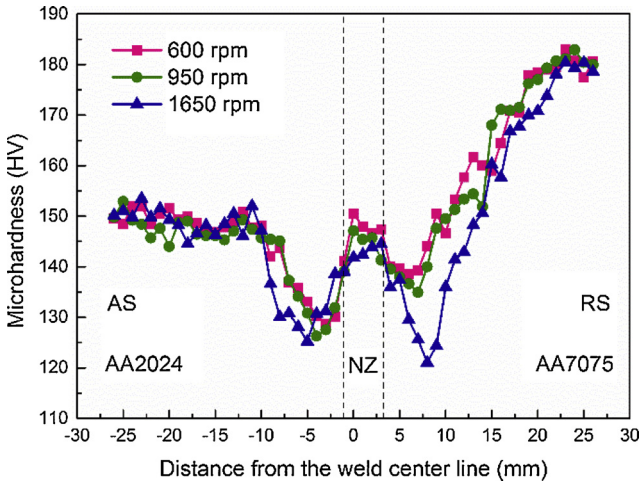

Fig. 14. Micro-hardness profiles along the center line of the thickness in the joints.

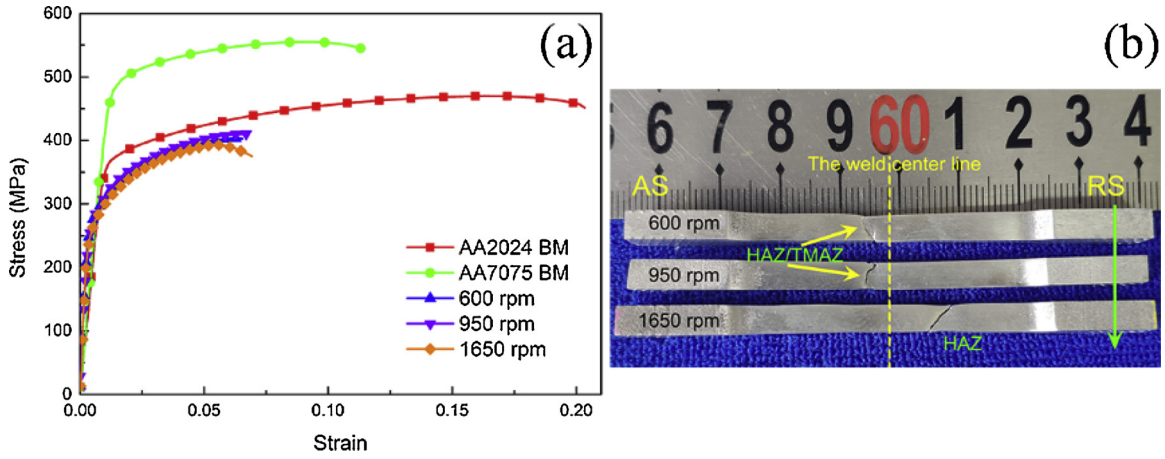

Fig. 15. Tensile data of the BMs and the joints with different rotational speeds (a) tensile curves and (b) fracture locations of the dissimilar FSW joints.

3.3. Mechanical behavior

3.3.1. Hardness test

Fig. 14 exhibits the hardness profile along the mid-thickness of the cross-section in the dissimilar joints at three rotational speeds. Clearly, the hardness profile of all the joints show asymmetric distribution with a typical "W" shape, which is similar to that found in AA7020/6060 FSW joints [48]. The inhomogeneous microstructure in the NZ is generated due to the asymmetry of FSW [7], resulting in conspicuous fluctuation in the hardness value, which results from the difference in the microstructure characterization controlled by welding parameters. The lower hardness values can be found in the AS/RS-HAZ due to the coarsening (Fig. 4c and f) and re-precipitation (Fig. 5b and d) of the second phases in the two BMs under thermal cycle. Despite of the welding parameters, a softening behavior exists in the NZ, and the hardness value of which is lower than that of the BMs. This is by reason of the fact that the NZ undergoes violent plastic deformation and intensive heat input, leading to the dissolution and re-precipitation of second phases, finally causing the lower hardness value. Besides, the hardness value in the NZ decreases with the increment of rotational speed, due to higher coarsening degree of second phases at higher temperature produced by increasing rotational speed. Additionally, a wider TMAZ and HAZ on the AS and RS are developed with the increment of tool rotational speed from 600 and 1650 rpm, which is related to higher peak temperature and exposure time.

3.3.2. Tensile behavior

The tensile curves of the two BMs and the dissimilar joints are displayed in Fig. 15a. Table 3 summarizes the tensile results. Compared with two BMs, all the values of yield strength (YS), ultimate tensile strength (UTS) and tensile elongation (TE) are lower in the dissimilar joints, indicating that the welding process deteriorates tensile performances of the dissimilar joints. The welding efficiency (i.e., a ratio of the UTS of the FSW joints to that of the AA2024 BM) is usually used to assess the mechanical performance of the joints. Higher welding efficiency signifies better performance of the joints. Apparently, the maximum UTS of 411.4 MPa (about 87.6 % of AA2024 BM) can be achieved in the joint produced at 950 rpm. The TE of three joints has no evident difference with the increment of rotational speed. The UTS increases first and then decreases with the increase of the rotational speed. This is associated with the heat input during FSW. Lower rotational speed causes less heat and then results in poor material mixing, while higher rotational speed produces more heat, leading to coarsening or dissolution of strengthening precipitates at the welded zone.

Table 3
Tensile test results of the BMs and the joints.

Materials	YS/MPa	UTS/MPa	TE/%	Fraction locations	Efficiency
2024 BM	360	470	20.3	–	–
7075 BM	476	555	11.4	–	–
600 rpm	276.6	403.8	6.53	AS-HAZ	85.9 %
950 rpm	274.9	411.4	6.75	AS-HAZ	87.6 %
1650 rpm	258.9	393.2	6.94	RS-HAZ	83.7 %

The failure locations of the joints are illustrated in Fig. 15b. It can be observed that the failure occurs in the AS-HAZ at 600 and 950 rpm while higher rotational speeds (1650 rpm) could shift the fracture to the RS-HAZ, which corresponds to the lowest hardness values in Fig. 14. The fracture mechanism of the dissimilar joints has been studied based on the characterization of fractured surface as shown in Fig. 16. Many circular and oval dimples with different sizes are distributed in the fracture surface of AA2024 BM (Fig. 16a), indicating ductile fracture mode. On the contrary, the fracture surface of AA7075 BM contains many smooth cleavage surfaces (Fig. 16b), indicating brittle fracture mode. Fig. 16c–h demonstrate that a large number of dimples are distributed in the fracture surface of the three joints, which shows similar fracture morphologies and also consistent with the results of TE in Table 3. Moreover, some particles can be found inside the dimples (marked by the red arrows in Fig. 16). These particles could offer the right conditions for crack nucleation, resulting in the lower strength and ductility (Fig. 15 and Table 3).

3.4. Corrosion behavior

Fig. 17 displays dynamic polarization curves of the BMs and NZ samples. The data of E_{corr} and I_{corr} are summarized in Table 4. It is found that all the three joints have similar E_{corr}, which is lower than that of the BMs. However, the E_{corr} is a thermodynamic parameter, which only reflects the corrosion tendency of the metals, but can't indicate the corrosion rate. I_{corr} is usually utilized to determine the corrosion resistance of materials. Lower I_{corr} indicates higher corrosion resistance. It can be observed from Table 4 that the I_{corr} of the joints at three rotational speeds is significantly higher than that of the two BMs. This is mainly because of the occurrence of galvanic corrosion in the welded zone. The potential difference between the two BMs is about 147 mV, which is obviously greater than 50 mV can be regarded as the existence of galvanic corrosion [49], resulting in higher corrosion rate in the welded area.

Furthermore, the results of Table 4 indicate that the I_{corr} of the joints at 600 and 1650 rpm is obviously higher than that of the joint fabricated at 950 rpm. The corrosion morphologies of the NZ in the joints at different rotational speeds are shown in Fig. 18. Through comparative analysis on the number and density of corrosion pits, the joints at 600 and 1650 rpm are corroded more seriously than that of the joint at

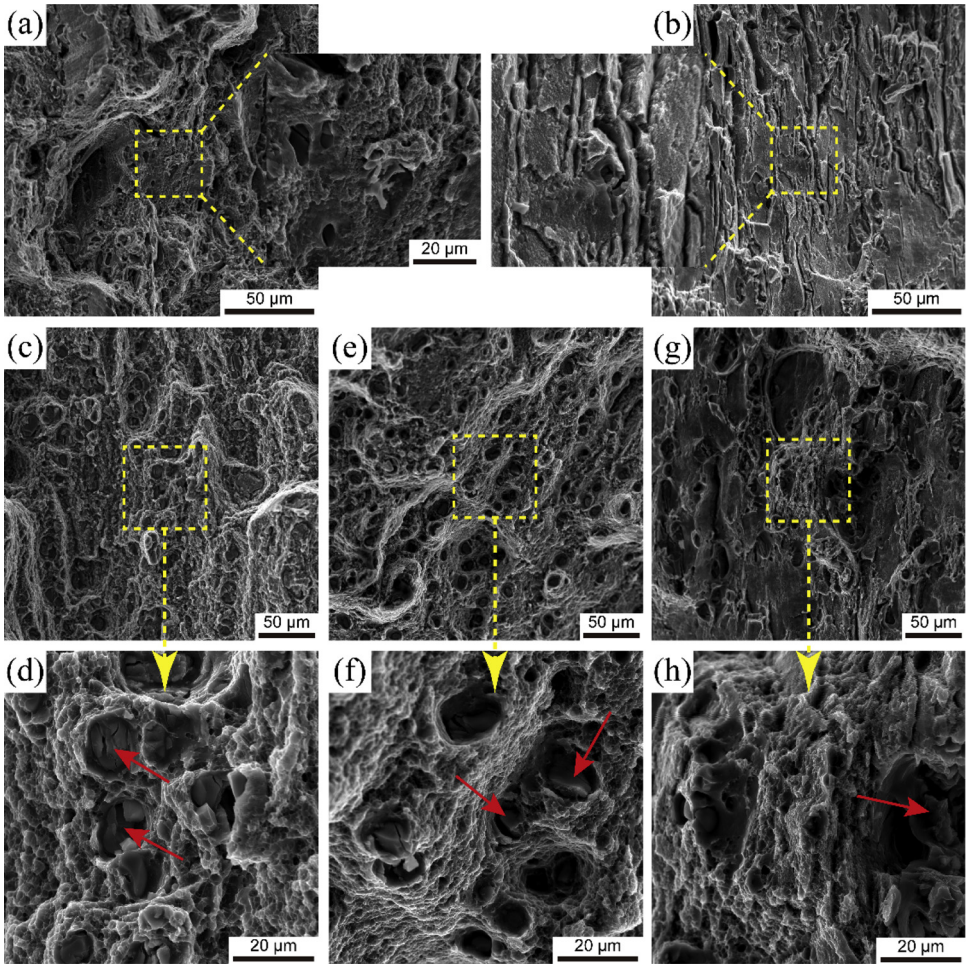

Fig. 16. Fracture surfaces of the BMs and the joints: (a) 2024 BM, (b) 7075 BM, (c & d) 600 rpm, (e &f) 950 rpm and (g & h) 1650 rpm.

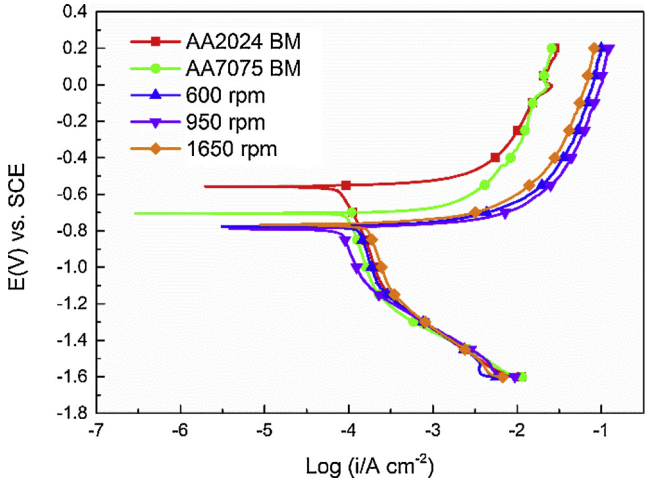

Fig. 17. Polarization curves of the BMs and the NZ of the dissimilar FSW welds.

Table 4
Polarization parameters of the BMs and the NZ of the joints.

Specimens	φ_{corr} (vs SCE)/V	J_{corr}/(μA·cm^{-2})
2024 BM	−0.557	71.5
7075 BM	−0.704	90.2
600 rpm	−0.777	129.6
950 rpm	−0.789	104.7
1650 rpm	−0.760	149.6

950 rpm. Consequently, the corrosion resistance of the joints at 950 rpm is higher than that of the joints at 600 and 1650 rpm. which is in accordance with the results of Li et al. [50]. A lower rotation speed (i.e., 600 rpm in this investigation) causes lower agitation and fragmentation effect for precipitation, while a higher rotation speed (i.e., 1650 rpm in this investigation) results in coarser second phases and grains due to higher peak temperature produced by higher rotational speed [51]. Niu et al. [52] and Kangazian [53] also found that the grain microstructure and the second phases in the NZ affect the corrosion resistance of the dissimilar FSW joints. Thus, sound joints are produced by appropriate rotational speed (i.e., 950 rpm in this study), in which both dispersoids and precipitates are generated to effectively restrain corrosion attack [50].

4. Conclusions

The dissimilar FSW AA2024-7075 joints were successfully obtained using different rotational speeds, and the local microstructure evolution in the NZ, mechanical properties and corrosion behavior of the dissimilar joints were studied. Some conclusions can be drawn from this study:

1) Due to severe plastic deformation and high-temperature exposure, dynamically recrystallization takes place in the NZ, forming fine equiaxed grains. The average grain size of all the SZ, CZ, BZ and IZ increases with increasing the rotational speed.
2) Shear textures are produced in the NZ compared to that of the BMs. Due to uneven shear deformation and heat input at different

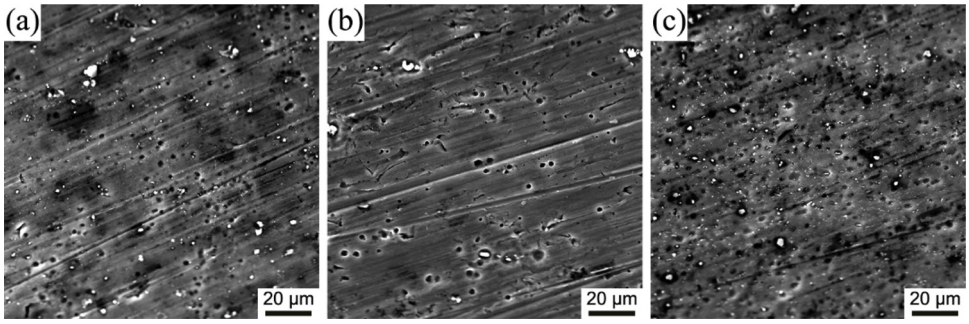

Fig. 18. Corrosion morphologies of AA2024 side in the welded zone of the welds at (a) 600 rpm, (b) 950 rpm and (c) 1650 rpm.

positions in the NZ, different types of texture components are formed and vary with the rotational speed.

3) Apparently asymmetric microhardness profile presents in the NZ and the failure of the joints is basically located in the lowest hardness zone during tensile tests.
4) The maximum UTS of 411.4 MPa (about 87.6 % of AA2024 BM) can be obtained in the joint at 950 rpm and the welding efficiency is about 87.6 % of AA2024 BM.
5) Higher corrosion current density presents in the welded zone due to the occurrence of galvanic corrosion. The corrosion behavior of the NZ mainly depends on the rotational speed and the joint fabricated at 950 rpm demonstrates higher corrosion performance.

Declaration of Competing Interest

We declare that we do not have any commercial or associative interest that represents a conflict of interest in connection with the work submitted.

Acknowledgements

We would like to greatly acknowledge the “National Natural Science Foundation of China” (NO. 51421001), “Fundamental Research Funds for the Central Universities” (NO. 106112018CDXYCL0018 and No. 2018CDJDCL0019) for financial support.

References

[1] Dursun T, Soutis C. Recent developments in advanced aircraft aluminium alloys. Mater Des 2014;56:862–71.
[2] Çam G, İpekoğlu G. Recent developments in joining of aluminum alloys. Int J Adv Manuf Tech 2017;91:1851–66.
[3] Sutton MA, Yang B, Reynolds AP, Taylor R. Microstructural studies of friction stir welds in 2024-T3 aluminum. Mater Sci Eng A 2002;323:160–6.
[4] Mao Y, Ke L, Chen Y, Liu F, Xing L. Inhomogeneity of microstructure and mechanical properties in the nugget of friction stir welded thick 7075 aluminum alloy joints. J Mater Sci Technol 2018;34:228–36.
[5] Cam G, Mistikoglu S. Recent developments in friction stir welding of Al-alloys. J Mater Eng Perform 2014;23:1936–53.
[6] Ye Z, Huang J, Gao W, Zhang Y, Cheng Z, Chen S, et al. Microstructure and mechanical properties of 5052 aluminum alloy/mild steel butt joint achieved by MIG-TIG double-sided arc welding-brazing. Mater Des 2017;123:69–79.
[7] Mishra RS, Ma Z. Friction stir welding and processing. Mat Sci Eng R 2005;50:1–78.
[8] Zhang C, Huang G, Cao Y, Zhu Y, Liu Q. On the microstructure and mechanical properties of similar and dissimilar AA7075 and AA2024 friction stir welding joints: effect of rotational speed. J Manuf Process 2019;37:470–87.
[9] Zhang C, Huang G, Cao Y, Wu X, Huang X, Liu Q. Optimization of tensile and corrosion properties of dissimilar friction stir welded AA2024-7075 joints. J Mater Eng Perform 2019;28:183–99.
[10] Nandan R, DebRoy T, Bhadeshia H. Recent advances in friction-stir welding–process, weldment structure and properties. Prog Mater Sci 2008;53:980–1023.
[11] Zhang C, Cui L, Wang D, Liu Y, Liu C, Li H. The heterogeneous microstructure of heat affect zone and its effect on creep resistance for friction stir joints on 9Cr–1.5 W heat resistant steel. Scr Mater 2019;158:6–10.
[12] Wang G, Zhao Y, Hao Y. Friction stir welding of high-strength aerospace aluminum alloy and application in rocket tank manufacturing. J Mater Sci Technol 2018;34:73–91.
[13] Ma Z, Feng A, Chen D, Shen J. Recent advances in friction stir welding/processing of aluminum alloys: microstructural evolution and mechanical properties. Crit Rev Solid State 2018;43:269–333.
[14] Zhang C, Huang G, Cao Y, Zhu Y, Li W, Wang X, et al. Microstructure and mechanical properties of dissimilar friction stir welded AA2024-7075 joints: influence of joining material direction. Mater Sci Eng A 2019:138368.
[15] Khan NZ, Siddiquee AN, Khan ZA, Mukhopadhyay AK. Mechanical and microstructural behavior of friction stir welded similar and dissimilar sheets of AA2219 and AA7475 aluminium alloys. J Alloys Compd 2017;695:2902–8.
[16] Prime MB, Gnäupel-Herold T, Baumann JA, Lederich RJ, Bowden DM, Sebring RJ. Residual stress measurements in a thick, dissimilar aluminum alloy friction stir weld. Acta Mater 2006;54:4013–21.
[17] Cavaliere P, Nobile R, Panella F, Squillace A. Mechanical and microstructural behaviour of 2024–7075 aluminium alloy sheets joined by friction stir welding. Int J Mach Tools Manuf 2006;46:588–94.
[18] Da Silva A, Arruti E, Janeiro G, Aldanondo E, Alvarez P, Echeverria A. Material flow and mechanical behaviour of dissimilar AA2024-T3 and AA7075-T6 aluminium alloys friction stir welds. Mater Des 2011;32:2021–7.
[19] Khodir SA, Shibayanagi T. Friction stir welding of dissimilar AA2024 and AA7075 aluminum alloys. Mater Sci Eng B 2008;148:82–7.
[20] Khodir SA, Shibayanagi T. Microstructure and mechanical properties of friction stir welded dissimilar aluminum joints of AA2024-T3 and AA7075-T6. Mater Trans 2007;48:1928–37.
[21] Venkateswarlu D, Mahapatra M, Harsha S, Mandal N. Processing and optimization of dissimilar friction stir welding of AA 2219 and AA 7039 alloys. J Mater Eng Perform 2015;24:4809–24.
[22] Hasan MM, Ishak M, Rejab M. Influence of machine variables and tool profile on the tensile strength of dissimilar AA7075-AA6061 friction stir welds. Int J Adv Manuf Tech 2017;90:2605–15.
[23] Reza-E-Rabby M, Tang W, Reynolds A. Effect of tool pin features on process response variables during friction stir welding of dissimilar aluminum alloys. Sci Technol Weld Join 2015;20:425–32.
[24] Upadhyay P, Reynolds A. Effect of backing plate thermal property on friction stir welding of 25-mm-thick AA6061. Metall Mater Trans A 2014;45:2091–100.
[25] Saravanan V, Rajakumar S, Banerjee N, Amuthakkannan R. Effect of shoulder diameter to pin diameter ratio on microstructure and mechanical properties of dissimilar friction stir welded AA2024-T6 and AA7075-T6 aluminum alloy joints. Int J Adv Manuf Tech 2016;87:3637–45.
[26] Saravanan V, Banerjee N, Amuthakkannan R, Rajakumar S. Microstructural evolution and mechanical properties of friction stir welded dissimilar AA2014-T6 and AA7075-T6 aluminum alloy joints. Metallogr Microstruct Anal 2015;4:178–87.
[27] Hasan MM, Ishak M, Rejab M. Effect of backing material and clamping system on the tensile strength of dissimilar AA7075-AA2024 friction stir welds. Int J Adv Manuf Tech 2017;91:3991–4007.
[28] Rodriguez R, Jordon J, Allison P, Rushing T, Garcia L. Corrosion effects on fatigue behavior of dissimilar friction stir welding of high-strength aluminum alloys. Mater Sci Eng A 2019;742:255–68.
[29] Fattah-alhosseini A, Naseri M, Gholami D, Imantalab O, Attarzadeh F, Keshavarz M. Microstructure and corrosion characterization of the nugget region in dissimilar friction-stir-welded AA5083 and AA1050. J Mater Sci 2019;54:777–90.
[30] Beyerlein IJ, Tóth LS. Texture evolution in equal-channel angular extrusion. Prog Mater Sci 2009;54:427–510.
[31] Fonda R, Bingert J. Texture variations in an aluminum friction stir weld. Scr Mater 2007;57:1052–5.
[32] Li S, Beyerlein IJ, Bourke MA. Texture formation during equal channel angular extrusion of fcc and bcc materials: comparison with simple shear. Mater Sci Eng A 2005;394:66–77.
[33] Moradi MM, Aval HJ, Jamaati R, Amirkhanlou S, Ji S. Microstructure and texture evolution of friction stir welded dissimilar aluminum alloys: AA2024 and AA6061. J Manuf Process 2018;32:1–10.
[34] Humphreys FJ, Hatherly M. Recrystallization and related annealing phenomena. Elsevier; 2012.
[35] Huang K, Logé R. A review of dynamic recrystallization phenomena in metallic materials. Mater Des 2016;111:548–74.
[36] Carlone P, Palazzo GS. Influence of process parameters on microstructure and mechanical properties in AA2024-T3 friction stir welding. Metallogr Microstruct Anal 2013;2:213–22.
[37] Chang C, Lee C, Huang J. Relationship between grain size and Zener–Holloman parameter during friction stir processing in AZ31 Mg alloys. Scr Mater

2004;51:509–14.
[38] Ghosh M, Kumar K, Mishra R. Analysis of microstructural evolution during friction stir welding of ultrahigh-strength steel. Scr Mater 2010;63:851–4.
[39] Ghosh M, Husain MM, Kumar K, Kailas S. Friction stir-welded dissimilar aluminum alloys: microstructure, mechanical properties, and physical state. J Mater Eng Perform 2013;22:3890–901.
[40] Wright SI, Nowell MM, Field DP. A review of strain analysis using electron backscatter diffraction. Microsc Microanal 2011;17:316–29.
[41] Herrera C, Ponge D, Raabe D. Design of a novel Mn-based 1 GPa duplex stainless TRIP steel with 60% ductility by a reduction of austenite stability. Acta Mater 2011;59:4653–64.
[42] Barnett M. A Taylor model based description of the proof stress of magnesium AZ31 during hot working. Metall Mater Trans A 2003;34:1799–806.
[43] Chen J, Fujii H, Sun Y, Morisada Y, Ueji R. Fine grained Mg–3Al–1Zn alloy with randomized texture in the double-sided friction stir welded joints. Mater Sci Eng A 2013;580:83–91.
[44] Liu Q, Jensen DJ, Hansen N. Effect of grain orientation on deformation structure in cold-rolled polycrystalline aluminium. Acta Mater 1998;46:5819–38.
[45] Calcagnotto M, Ponge D, Demir E, Raabe D. Orientation gradients and geometrically necessary dislocations in ultrafine grained dual-phase steels studied by 2D and 3D EBSD. Mater Sci Eng A 2010;527:2738–46.
[46] Rahimi S, Konkova T, Violatos I, Baker T. Evolution of microstructure and crystallographic texture during dissimilar friction stir welding of duplex stainless steel to low carbon-manganese structural steel. Metall Mater Trans A 2019;50:664–87.
[47] Shen J, Wang F, Suhuddin UF, Hu S, Li W, Dos Santos JF. Crystallographic texture in bobbin tool friction-stir-welded aluminum. Metall Mater Trans A 2015;46:2809–13.
[48] Giraud L, Robe H, Claudin C, Desrayaud C, Bocher P, Feulvarch E. Investigation into the dissimilar friction stir welding of AA7020-T651 and AA6060-T6. J Mater Process Technol 2016;235:220–30.
[49] Schneider M, Kremmer K, Lämmel C, Sempf K, Herrmann M. Galvanic corrosion of metal/ceramic coupling. Corros Sci 2014;80:191–6.
[50] Li N, Li W, Xu Y, Yang X, Alexopoulos ND. Influence of rotation speed on mechanical properties and corrosion sensitivity of friction stir welded AA2024-T3 joints. Mater Corros 2018;69:1016–24.
[51] Xu W, Liu J. Microstructure and pitting corrosion of friction stir welded joints in 2219-O aluminum alloy thick plate. Corros Sci 2009;51:2743–51.
[52] Niu P, Li W, Li N, Xu Y, Chen D. Exfoliation corrosion of friction stir welded dissimilar 2024-to-7075 aluminum alloys. Mater Charact 2019;147:93–100.
[53] Kangazian J, Shamanian M, Ashrafi A. Surface characterization of incoloy 825 Ni-Based Alloy/2507 super duplex stainless steel dissimilar friction stir welds. Corrosion 2018;74:1259–71.